

Diverse Magnetic Phase Diagram and Anomalous Hall Effect in Antiferromagnetic LuMn_6Sn_6

Shirin Mozaffari,^{1,*} Seung-Hwan Do,¹ Richa P. Madhogaria,¹ Aikaterini Flessa Savvidou,² Brian W. Casas,² William R. Meier,¹ Rui Xue,³ Eun Sang Choi,² Luis Balicas,² and David G. Mandrus^{1,3,†}

¹*Department of Materials Sciences and Engineering,
The University of Tennessee, Knoxville, TN 37996, USA*

²*National High Magnetic Field Laboratory, Florida State University, Tallahassee, Florida 32310, USA*

³*Department of Physics and Astronomy, The University of Tennessee, Knoxville, TN 37996, USA*

(Dated: March 18, 2025)

The interactions between conduction electrons and magnetism can significantly enhance the Hall signal, a phenomenon known as the anomalous Hall effect (AHE). While the AHE is generally not expected in antiferromagnets with vanishing magnetization, a large AHE is observed in certain antiferromagnets with noncollinear spin textures and nonvanishing Berry curvature. In this work, we present a rich temperature and magnetic phase diagram with eight distinct magnetic phases for the antiferromagnetic kagome compound LuMn_6Sn_6 . In the coplanar canted antiferromagnetic phase, we observe an AHE, which likely originates from the intrinsic effects. Upon entering the ferromagnetic phase, the AHE significantly increases and exceeds the conventional limits of AHE of intrinsic origin. Additionally, we observe a topological Hall effect (THE) that emerges in the conical magnetic phase. Notably, the THE in LuMn_6Sn_6 persists over an extended magnetic field range of up to 25 T. Our detailed transport measurements highlight the need for theoretical modeling to explain the observations of AHE and THE in RMn_6Sn_6 (R = Rare earth) family of compounds.

I. INTRODUCTION

The electrical Hall effect serves as a widely used probe to explore topological effects in magnetic systems. The Hall current requires breaking time-reversal symmetry. When this symmetry is broken by an external magnetic field, it results in the ordinary Hall effect (OHE). Alternatively, the magnetic field can induce internal magnetization, resulting in an additional contribution to the Hall current, referred to as the anomalous Hall effect (AHE)[1, 2]. Intrinsic contributions to the AHE originate from the Berry curvature of the Bloch wave function, summed over all occupied states, analogous to the mechanism of the quantum Hall effect.

In ferromagnets with spontaneous magnetization, AHE can arise without the presence of an external magnetic field. Traditionally, the Hall effect has not been associated with antiferromagnetic order. However, recent theoretical and experimental studies have revealed significant Hall effects in certain magnetic crystals lacking global magnetization. Examples include the observation of a Hall effect in a spin-liquid candidate $\text{Pr}_2\text{Ir}_2\text{O}_7$ [3], certain non-collinear antiferromagnetic compounds such as Mn_3Sn , Mn_3Ge , MnGe , NbMnP , and Ce_2CuGe_6 [4–8], and the newly discovered Hall effect in altermagnetic materials [9]. Remarkably, the AHE in some of these antiferromagnets is comparable in strength to that observed in ferromagnets.

These discoveries led us to move away from viewing the Hall effect solely as arising from conventional symmetry-

breaking processes. Instead, the Hall response is now understood to be closely tied to non-trivial topology in the electronic structure, resulting in an enhanced response that challenges the traditional paradigm of scaling with total magnetization strength [2].

In addition to the ordinary and anomalous Hall effects, noncoplanar spin alignments in real space can give rise to a finite scalar spin chirality, $\chi_{ijk} \sim s_i \cdot (s_j \times s_k)$, where $s_{i,j,k}$ are the spin moments of neighboring sites. This spin chirality can act as a local emergent magnetic field for conduction electrons, leading to a transverse response, termed the topological Hall effect (THE).

Among the numerous compounds with magnetic topological behavior, the family of kagome structure materials is a quintessential embodiment of the concept. Examples include Fe_3Sn_2 [10, 11], Fe_3Sn [12], Mn_3X ($X = \text{Sn, Ge, Pt, Rh, Ir}$) [4, 13, 14], $\text{Co}_3\text{Sn}_2\text{S}_2$ [15], and the family of RMn_6Sn_6 (R = Rare earth) [16]. The latter lattice, which is strongly frustrated, is the focus of this paper.

RMn_6Sn_6 family materials consists of kagome bilayers of Mn atoms that are separated by Sn and R atoms along the c axis. The family shows a collinear ferrimagnetic ground state with magnetic rare earths $R = \text{Gd-Er}$ due to the strong antiferromagnetic (AF) coupling between R and Mn atoms [18–25]. The non-magnetic rare earth analogues, $R = \text{Sc, Y, Lu}$, are antiferromagnets and consist of ferromagnetic (FM) double layers of the Mn kagome plane, which antiferromagnetically couple with neighboring bilayers [26–29].

RMn_6Sn_6 is reported to have several field-induced magnetic phases, and the observation of THE in one of these phases in $R = \text{Y, Sc, Er}$ is among the most exciting phenomena reported for this family [21, 30–32]. Beyond THE, RMn_6Sn_6 compounds have demonstrated other in-

* smozaff1@utk.edu

† dmandrus@utk.edu

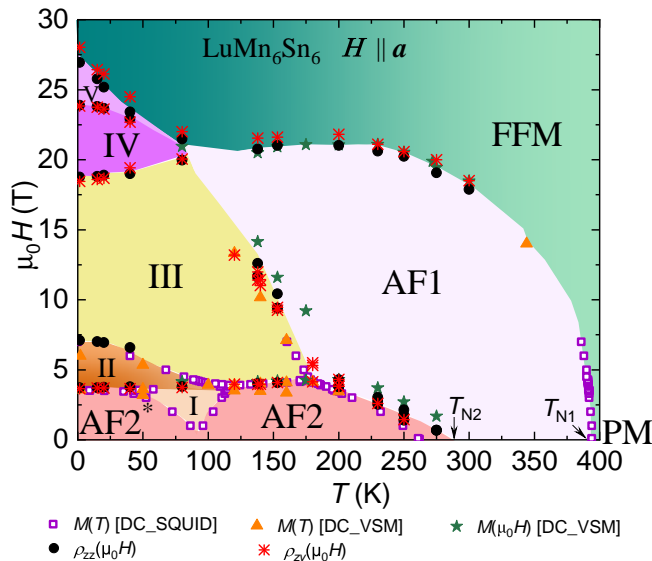


FIG. 1. Temperature T and magnetic field $\mu_0 H$ phase diagram of LuMn_6Sn_6 labeled for the various magnetic phases for field applied parallel to a -axis, including two different antiferromagnetic (AF1 and AF2) and forced ferromagnetic (FFM) states. The magnetic structures of phases labeled by Roman numbers are defined in Ref. [17]. The (H, T) phase diagram is constructed from DC magnetization (M), longitudinal (ρ_{zz}) and Hall resistivity (ρ_{zy}) measurements under an external field along the crystalline a axis.

triguing phenomena, including magnetization-driven Lifshitz transitions [33], a large anomalous transverse thermoelectric effect [34], and topological Nernst and thermal Hall effects [35, 36].

Among the members of RMn_6Sn_6 , LuMn_6Sn_6 is studied the least likely because of the very strong field required to induce the fully polarized state. Here, in this study, shown in Fig. 1, we report a rich field and temperature phase diagram for LuMn_6Sn_6 with the magnetic field applied along the crystalline a -axis. Such a rich phase diagram is rare and indicates the presence of interactions and competition between multiple orders. We identified eight different magnetic phases as a result of competition between FM and AF coupling between Mn kagome layers. This is more diverse than the Y and Sc sister compounds. To label the numerous magnetic phases, Roman numerals are used throughout this paper.

In addition to the rich magnetic phase diagram, our Hall effect measurements show an AHE in the canted antiferromagnetic AF1 state and a THE in phase III (most likely a transverse conical phase phase). Moreover, our study underscores the importance of considering anisotropic magnetoresistance and advocates for theoretical models over empirical relations in the analysis of nontrivial Hall responses. LuMn_6Sn_6 is ordered at room temperature and thus potentially has a direct application in the design of complex magnets for data storage.

II. EXPERIMENTAL DETAILS

Crystals of LuMn_6Sn_6 were grown from a tin flux using an atomic ratio of Lu:Mn:Sn = 1:6:30. The Lu pieces (Alfa Aesar 99.9%), Mn pieces (Alfa Aesar 99.95%) and the Sn shot (Alfa Aesar 99.9999%) were loaded into an alumina crucible. The crucible assembly was sealed in a fused silica ampule and heated to 973 °C over 12 h, then held for 12 h. The mixture was then cooled to 923 °C at a rate of 2.5 °C/h, followed by heating to 963 °C over 2 h. Finally, it was cooled to 600 °C at a rate of 1.5 °C/h. At this temperature, the flux was separated from the crystals by inverting the tube and centrifuging. This process yielded blocky hexagonal crystals up to 1 cm in size [Fig. 2(a)]. The additional heating step to 963 °C was included to promote the growth of larger crystals. The crystal structure was verified by grinding a small amount of the crystals into powder. Powder X-Ray Diffraction measurement was performed using a Bruker D2 Phaser equipped with a $\text{Cu } K_\alpha$ X-ray source at the Institute for Advanced Materials & Manufacturing (IAMM) Diffraction facility, located at the University of Tennessee, Knoxville. Fig. S1 within the Supplemental Material (SM) [37] confirms the $P6/mmm$ HfFe_6Ge_6 -type structure of the sample. Conventional magnetotransport experiments were performed in a physical property measurement system (PPMS-Quantum Design) under magnetic fields up to 14 T and temperatures as low as 1.8 K. Magnetization measurements under fields up to 7 T were performed in a commercial superconducting quantum interference device magnetometer (SQUID-Quantum Design). The high magnetic field magnetotransport measurements were performed in a resistive Bitter magnet at the National High Magnetic Field Laboratory (NHMFL) in Tallahassee, FL, under continuous fields up to 35 T. The measured longitudinal and transverse resistivities were field-symmetrized and antisymmetrized, respectively, to correct the effect of contact misalignment.

III. RESULTS AND DISCUSSION

A. Crystal Structure Analysis

LuMn_6Sn_6 has a hexagonal structure with space group $P6/mmm$ (No. 191), as shown in Fig. 2(b). The structure can be viewed as stacking layers of Lu, Mn, and Sn. Within each unit cell there are three different Sn sites (Sn1, Sn2, and Sn3) and two non-equivalent kagome planes of Mn atoms which are separated by different layers of LuSn3 and Sn1-Sn2-Sn1. Only Mn atoms possess magnetic moments which are aligned ferromagnetically within the ab -planes of the hexagonal lattice; the average of which in each Mn layer is shown schematically with an orange arrow in Fig. 2(c). Neutron diffraction in zero external magnetic field shows that the Mn layers across the Sn1-Sn2-Sn1 layers are coupled ferromagnetically but the coupling through the Lu-Sn3 layer is antiferromag-

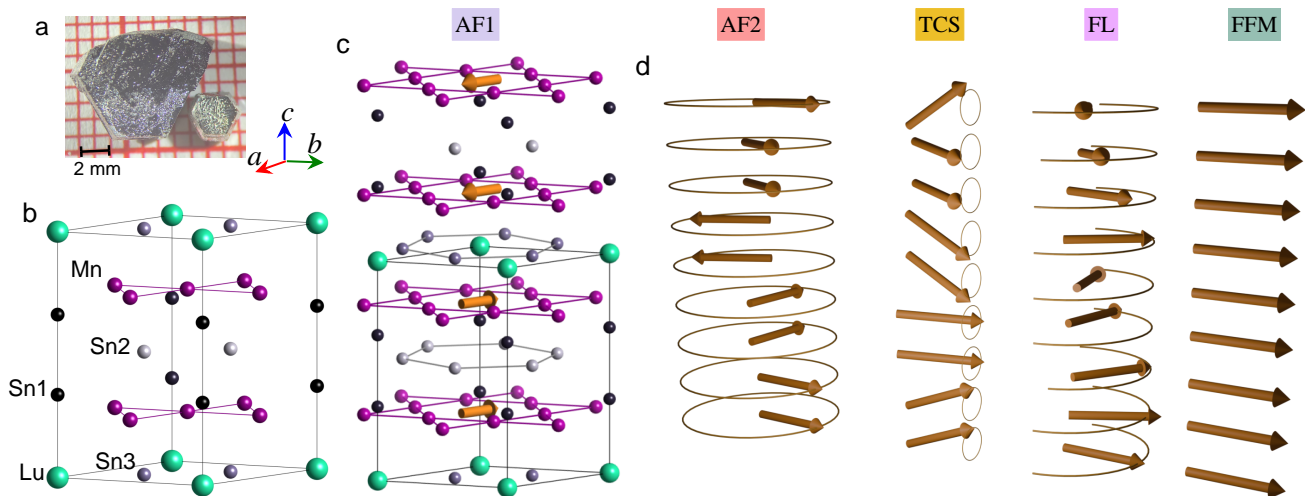


FIG. 2. (a) A picture of typical hexagonal prismatic LuMn_6Sn_6 crystals. (b) Sketch of LuMn_6Sn_6 structure generated with Vesta. The boxed area shows the primitive cell of the crystal structure. The three Sn positions are shown with three different shades of grey color. (c) Room temperature magnetic structures (AF1 phase) of LuMn_6Sn_6 at zero field based on the neutron diffraction measurements [27]. For simplicity, the magnetization of each manganese kagome sheet is shown by an arrow in the middle. (d) Sketch of different magnetic structures for YMn_6Sn_6 induced by a field applied along the a crystalline axis [30].

TABLE I. Lattice parameters and the Néel temperatures for RMn_6Sn_6 , $R = \text{Sc}, \text{Y}, \text{Lu}$. T_{N1} marks the transition to a collinear antiferromagnetic state and T_{N2} is a transition to an incommensurate spiral state. ScMn_6Sn_6 lacks the collinear antiferromagnetic state.

R	a (Å)	c (Å)	T_{N1} (K)	T_{N2} (K)	References
Sc	5.465	8.961	384	–	[35]
Lu	5.508	8.989	395	263	This study
Y	5.541	9.035	345	–	[30]
	5.512	8.984	359	326	[38]
	5.541	9.023	340	333	[39]

netic [26, 27], as depicted in Fig. 2(c). This makes the magnetic unit cell in the AF1 phase twice the size of the chemical unit cell. The general magnetic structure in the RMn_6Sn_6 ($R = \text{Sc}, \text{Lu}, \text{Y}$) family and the band topology depend on the R element type. Table I summarizes the lattice parameters and Néel temperatures in this family. The a and c lattice parameters of the Lu compound are in between the Sc and Y compound.

B. Magnetic Properties

Zero field Neutron scattering experiments on LuMn_6Sn_6 and YMn_6Sn_6 show that below the Néel temperature T_{N1} , a commensurate collinear AF structure forms first with the propagation vector $k = (0, 0, 1/2)$ [26, 27, 39, 40]. This is the magnetic configuration of phase AF1, which is the dominant phase in the (H, T) phase diagram in Fig. 1. As the field increases, the moments gradually cant within the ab -plane, forming

the coplanar canted AF1 state [17, 39, 40]. Upon cooling to T_{N2} , an incommensurate magnetic phase appears and becomes the only phase below this temperature [26–29, 39, 40]. This incommensurate phase has two nearly equal wave vectors and is known as a double-flat spiral or a distorted spiral (DS). In this c -axis helical order, the Mn moments in each bilayer rotate by a non-constant angle, requiring two distinct rotation angles to describe the directions of the magnetic moments [41]. For YMn_6Sn_6 , the resulting complex arrangement with a non-uniform rotation of the moments leads to a supercell structure with $c' = 36c$ [26]. For LuMn_6Sn_6 this incommensurate phase corresponds to the AF2 phase, as shown in Fig. 1.

Upon application of an external magnetic field in the ab -plane, the magnetic structure becomes more complex and several field-induced magnetic phases rise. In YMn_6Sn_6 , the field-induced magnetic phases are identified as distorted spiral (DS), transverse conical spiral (TCS), fan-like (FL), and forced ferromagnet (FFM) [30]. The cartoon in Fig. 3(d) schematically shows these phases. By comparing the magnetic phase diagrams of YMn_6Sn_6 [33, 39], it can be inferred that LuMn_6Sn_6 likely adopts a transverse conical spiral (TCS) and a fan-like (FL) magnetic structure in phases III and IV, respectively.

Figure 3(a) presents the temperature T dependence of magnetization M obtained for a magnetic field applied along a and c axis in LuMn_6Sn_6 . At a small field of 0.05 T, two phase transitions occurring at $T_{\text{N1}} = 395$ K and $T_{\text{N2}} = 263$ K manifest themselves as drops in magnetization, suggesting the antiferromagnetic character of the orderings. These two transitions are slightly higher than previously reported [29, 42]. We observed that the use of higher purity tin and manganese results in a change

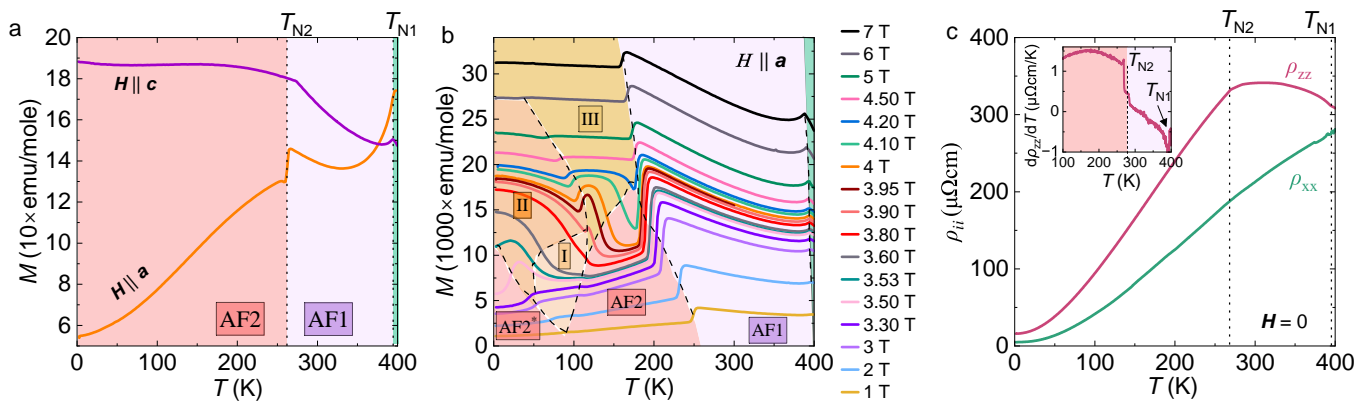


FIG. 3. (a) Magnetization M as a functions of temperature T for magnetic field $\mu_0 H = 0.05$ T applied parallel to a and c -axis of the LuMn_6Sn_6 crystal, obtained on heating the sample after zero-field-cooling (ZFC) down to ~ 2 K. (b) $M(T)$ curves measured under several different magnetic field values for $\mu_0 H$ applied along a axis. Dashed lines define the boundaries between different field-induced magnetic phases. (c) Electrical resistivity as a function of temperature, with the electric current applied along the a -axis (ρ_{xx}) and c -axis (ρ_{zz}) of the crystal. Inset shows the temperature derivative of ρ_{zz} in the vicinity of T_{N1} and T_{N2} . Dotted lines in (a) and (c) show antiferromagnetic transitions happening at T_{N1} and T_{N2} .

of T_N 's to slightly higher temperatures.

T_{N1} corresponds to a transition from a paramagnetic state to a canted antiferromagnetic state (AF1 phase), while at T_{N2} a transition to an incommensurate helical order (AF2 phase) with an in-plane ferromagnetic order occurs [26, 27], as explained at the beginning of this section. There is a slight difference between the Néel temperatures for the two orientations of the field. Our reported values are for measurements of $M(T)$ in which the field is applied along the a -axis.

LuMn_6Sn_6 exhibits rich magnetism at low temperatures and fields. When cooled below 200 K, it undergoes a series of magnetic phase transitions, as shown by the strong field dependence of M in phases AF2*, I, II, and III in Fig. 3(b). Phase I was not clearly distinguishable in the field-dependence measurements of magnetization and resistivity. Neutron scattering measurements by Do et al. [17] show a continued change in the ordering wave vector below 250 K and a distinct kink at 100 K. Therefore, we labeled the magnetic phase below 100 K by AF2* to communicate this discontinuity in the character of the wave vector.

The collinear antiferromagnetic state in YMn_6Sn_6 [38, 43] exists in a very narrow temperature range, as can be seen from the small temperature difference between T_{N1} and T_{N2} in Table I. This phase is absent in ScMn_6Sn_6 [35] which has a double flat spiral structure throughout the temperature range below its Néel temperature. However in LuMn_6Sn_6 the canted antiferromagnetic AF1 phase is much more extended the phase diagram [Fig. 1].

Direct comparison of the magnetic phase diagrams of LuMn_6Sn_6 , YMn_6Sn_6 [33, 39], and ScMn_6Sn_6 [32], reveals that the DS phase is divided into phases of I, II, AF2, and AF2* in the Lu compound. This is manifested in Fig. 3(b) by the strong response of the helical AF2 state to the magnetic field at lower temperatures. The

temperature derivative of the $M(T)$ isotherm curves was used to construct the phase diagram, as shown by the square-shaped data points in Fig. 1.

C. Electrical Transport Properties

The T dependence of the longitudinal resistivity in-plane (ρ_{xx}) and out-of-plane (ρ_{zz}) are shown in Fig. 3(c). The electric current was applied along the a -axis (c -axis) of the crystal to measure ρ_{xx} (ρ_{zz}). The antiferromagnetic transitions appear as steps and more clearly in the temperature derivative of ρ_{zz} , Fig. 3(c) inset. ρ_{zz} shows a negative concavity in the AF1 phase, which is uncommon for an itinerant antiferromagnet in its ordered state. This type of increase in electrical resistivity at the magnetic ordering temperature is commonly attributed to the formation of a superzone gap on the Fermi surface, where some part of the Fermi surface vanishes and hence the resistivity increases [44]. By further cooling below T_{N2} , ρ_{zz} shows a positive concavity, observed in the whole T range for ρ_{xx} , possibly due to the suppression of spin-disorder scattering. We obtained residual resistivity ratios $RRR = \frac{R_{300\text{K}}}{R_{2\text{K}}} = 22 - 44$ and a residual resistivity of $RR = 4 - 15 \mu\Omega\text{cm}$ in different crystals.

The magnetotransport properties for the c -axis magnetic field are shown within SM [37]. The $M(T)$ curves for this direction do not show such a strong dependence on the magnetic field with no field-induced transition below 7 T. Therefore, this paper focuses on the magnetotransport properties with an in-plane magnetic field.

The intricate field dependence of the transport properties shown in Fig. 4 reveal several magnetic phases that are induced by the application of $H \parallel a$. The field derivatives of these curves were used in constructing the (H, T) phase diagram in Fig. 1 [detailed in

SM [37], Fig. S3]. The $M(H)$ isotherms in Fig. 4(a) resemble those of RMn_6Sn_6 ($R = \text{Sc}$ and Y), albeit with the common magnetic phases appearing at much larger fields [30, 32, 33, 45]. The abrupt change of M around 4 T in Fig. 4(a) (at AF2 to III boundary) suggests a first-order metamagnetic transition, which was seen in ScMn_6Sn_6 and YMn_6Sn_6 as well [30, 32]. At low temperatures M starts to saturate at $\mu_0 H > 25$ T, while for ScMn_6Sn_6 and YMn_6Sn_6 the FFM phase appears at $\mu_0 H > 3$ T and 10 T, respectively [30, 32, 33, 45]. The larger saturation field in LuMn_6Sn_6 indicates a stronger antiferromagnetic interlayer interaction compared to the other sister compounds.

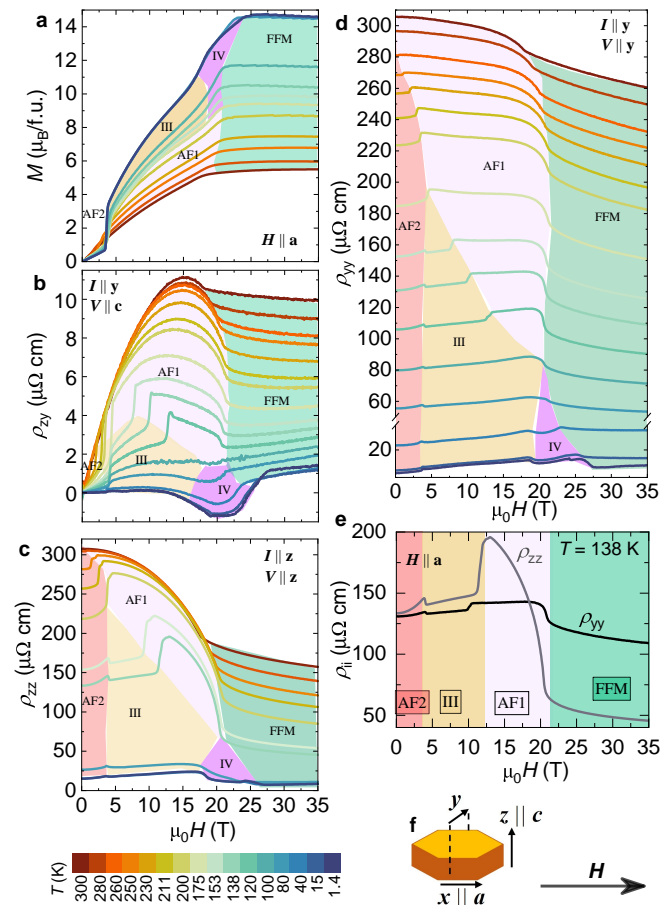


FIG. 4. Magneto-transport properties of LuMn_6Sn_6 in different crystallographic directions. (a) magnetization M , (b) Hall resistivity ρ_{zy} , (c) longitudinal resistivity ρ_{zz} , and (d) longitudinal resistivity ρ_{yy} as a function of magnetic field at various temperatures. (e) Magnetoresistivity shows a strong anisotropy in the AF1 phase. The cartoon in (f) shows the directions of the applied electrical current, magnetic field, and the measured voltage. The different magnetic phases are colored and labeled according to Fig. 1. Magnetic field was applied along the a -axis in these measurements.

i in the electrical transport measurements ρ_{ji} , Fig. 4(b)–(e), indicates the direction in which the electric current was applied and j indicates the direction of

the measured voltage. Fig. 4(f) schematically shows this configuration. Fig. 4(c) and (d) show that both longitudinal resistivities increase parabolically with H in the AF2 phase and linearly in phase III, while in the AF1 phase ρ_{zz} exhibit negative magnetoresistivity and ρ_{yy} shows minimal changes. Hall resistivity, shown in Fig. 4(b), appears to be more sensitive to phase transitions around AF1 and III than magnetization, showing a sudden increase, as the magnetic structure evolves. These sharp increases in ρ_{zy} are more pronounced at 120 K, 138 K, and 153 K and were consistently observed in multiple crystals and multiple batches.

In low fields, the field dependence of the Hall data have a positive slope, indicating that holes are the dominant charge carriers. We have obtained a rough estimate for the densities n and mobilities μ of the holes by fitting $\rho_{zy}(H)$ to a simple band Drude model, which are shown in Fig. S4 within the Supplemental Material (SM) [37]. At room temperature, we obtained $n_{300\text{K}} = 5.5 \times 10^{18} \text{ cm}^{-3}$ and $\mu_{300\text{K}} = 3721 \text{ cm}^2 \text{ V}^{-1} \text{ S}^{-1}$, which drop to smaller values at lower temperatures. We also observed distinct Shubnikov-de Haas (SdH) oscillations in ρ_{zz} at 1.4 K in the FFM phase for $\mu_0 H > 27$ T with the magnetic field aligned along the a -axis, shown in Fig. S5. The analysis of the SdH signal, as explained in the SM [37] revealed a Fermi surface pocket with a k -space area of $A_k = 7.2 \text{ nm}^{-2}$.

1. The Importance of Anisotropy

The Hall effect behavior in Fig. 4(b) is quite intriguing. At high temperatures, ρ_{zy} shows a hump in the AF1 phase that may mistakenly be regarded as THE. However, given the coplanar canted antiferromagnetic structure, the system is not expected to exhibit a THE in the AF1 phase. In this section, we show that we can obtain a large apparent THE in the AF1 phase if care is not taken in considering both longitudinal resistivities.

As shown in Fig. 4(c) and (d), in the canted AF1 phase, ρ_{zz} exhibits a strong negative magnetoresistivity, while the ρ_{yy} curves remain relatively flat. The strong anisotropy in the longitudinal resistivities in the AF1 phase is depicted in Fig. 4(e) for a representative temperature of 138 K. This pronounced anisotropy in the magnetoresistivities plays a critical role in the proper analysis of the Hall effect data, which is further discussed in the following.

The three main contributions to the Hall effect are the ordinary Hall effect $\rho_{zy}^O = R_0 B$ due to the Lorentz force (R_0 is the ordinary Hall coefficient and B is the induction field), the anomalous Hall resistivity $\rho_{zy}^A = R_s M \rho_{yy} \rho_{zz}$ (R_s is the coefficient of the conventional anomalous Hall resistivity), and the topological Hall resistivity ρ_{zy}^T ; $\rho_{zy} = \rho_{zy}^O + \rho_{zy}^A + \rho_{zy}^T$. The process of isolating these terms is detailed within SM [37].

The equations for AHE are empirical and is commonly expressed as $\rho_{xy}^A = R_s M \rho_{xx} \rho_{yy}$, where $\rho_{xx}(\rho_{yy})$ and ρ_{xy}

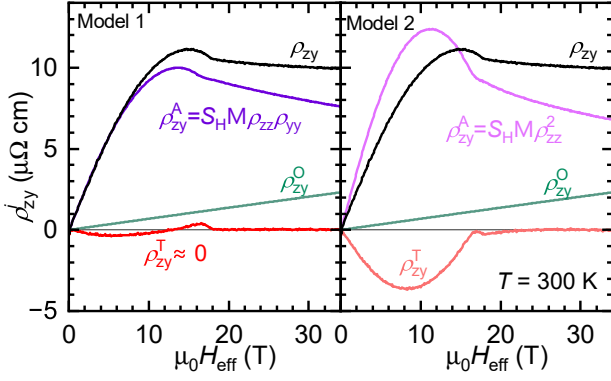


FIG. 5. Importance of considering anisotropy in the analysis of Hall effect. The anomalous Hall resistivity at 300 K for LuMn₆Sn₆ in the coplanar canted AF1 phase is estimated using two empirical relations (model 1 and 2). Both panels display the field dependence of Hall resistivity ρ_{zy} and its components: ρ_{zy}^O (ordinary), ρ_{zy}^A (anomalous), and ρ_{zy}^T (topological). In model 1, ρ_{zy}^A is derived by accounting for the anisotropy in the longitudinal resistivity. In model 2, ρ_{zy}^A is estimated to be equal to ρ_{zz} , leading to an exaggerated value for ρ_{zy}^T .

correspond to longitudinal and Hall resistivities, respectively [1]. ρ_{xy}^A is derived using Eq. III C 2 and assuming that anomalous Hall conductivity is proportional to magnetization. In most metallic systems, the in-plane resistivities are isotropic, making it reasonable to express $\rho_{xy}^A = R_s M \rho_{xx}^2$. However, in layered compounds with anisotropic resistivity, especially in out-of-plane measurements (zy-plane), if both longitudinal resistivities are not carefully considered, as shown in Fig. 5 by model 2, the resulting AHE may be overestimated. This overestimation of ρ_{zy}^A consequently leads to an exaggerated value of 4 $\mu\Omega$ cm for THE, which is larger than the values reported for well-established skyrmionic systems such as MnSi [46] and Gd₂PdSi₃ [47]. Note that at 300 K, the magnetic structure is coplanar canted antiferromagnet with zero scalar spin chirality and a THE is not expected. The need for a more thorough consideration in identifying emergent magnetic fields in frustrated itinerant magnets has recently been discussed by Refs. [48, 49] as well.

2. Anomalous Hall Effect in the canted AF1 and FFM phases

We further explore the Hall effect data by examining the conductivity σ_{zz} and Hall conductivity σ_{zy} , shown in Fig. 6. These curves were extracted by inverting the resistivity tensor [50].

$$\begin{bmatrix} \sigma_{yy} & \sigma_{yz} \\ \sigma_{zy} & \sigma_{zz} \end{bmatrix} = \begin{bmatrix} \rho_{yy} & \rho_{yz} \\ \rho_{zy} & \rho_{zz} \end{bmatrix}^{-1} = \frac{1}{\rho_{yy}\rho_{zz} + \rho_{zy}^2} \begin{bmatrix} \rho_{zz} & -\rho_{yz} \\ -\rho_{zy} & \rho_{yy} \end{bmatrix} \quad (1)$$

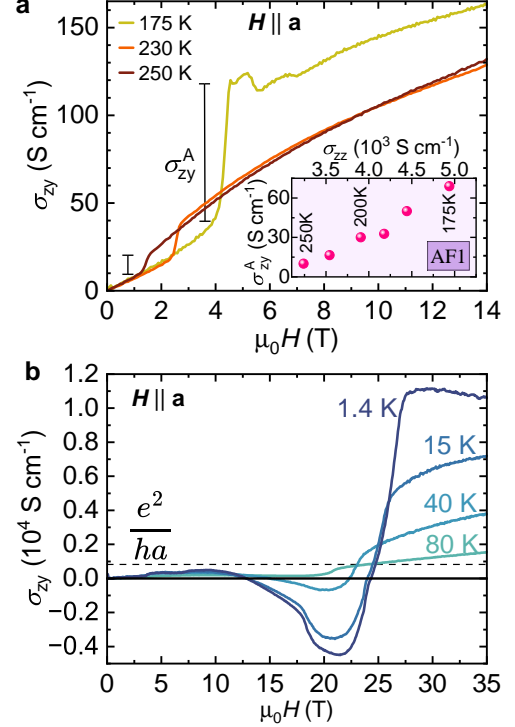


FIG. 6. Hall conductivity in LuMn₆Sn₆ as a function of magnetic field oriented along *a*-axis at high temperatures in the canted AF1 phase (a) and low temperatures (b). The vertical lines in (a) show the extracted anomalous contribution σ_{zy}^A to the Hall conductivity in the canted AF1 phase, which are plotted against conductivity in the inset. The upper threshold value of the intrinsic AHC in three-dimensions (e^2/ha) is indicated by the dashed line in (b).

The anomalous contribution to the Hall conductivity (AHC) in the AF1 phase, σ_{zy}^A , is read directly from the jumps in σ_{zy} values marked by the black vertical lines in Fig. 6(a). These values are plotted in the inset of Fig. 6(a) along with the conductivity values. The intrinsic AHE, which is related to the Berry curvatures in momentum space theoretically should be less than e^2/ha . Here, e is the elementary charge, h is Planck's constant, and a is the typical lattice parameter, which for LuMn₆Sn₆ would be ≈ 800 S cm⁻¹. The extracted σ_{zy}^A values in the inset of Fig. 6(a) are within the limit of the intrinsic AHC. Therefore, we conclude that the sudden increase in the ρ_{zy} values upon entering phase AF1 is due to intrinsic contributions to the AHE. The maximum value of σ_{zy}^A that we can unambiguously extract is about 70 S cm⁻¹ at 175 K. This is less than the typical values for intrinsic AHC in ferromagnets such as Fe (> 1000 S cm⁻¹) [51] or in itinerant *d*-electron AFM materials such as Mn₃Sn, Mn₃Ge, and NbMnP (100–450 S cm⁻¹) [4, 5, 7].

Another possible explanation for the sudden increase in the Hall effect data is the metamagnetic multiband Hall

effect [48]. In this scenario, the non-monotonic character of the Hall effect is attributed to a band-dependent mobility modulation resulting from $4f$ - $5d$ interactions. The Kondo-like Hamiltonian in this model is particularly effective at low temperatures and fields, while the sharp jump in ρ_{zy} occurs at high fields and relatively elevated temperatures.

We now turn the attention to the low temperature transport properties. Scaling relations between longitudinal and Hall conductivity are often employed empirically to identify the dominant scattering mechanisms that contribute to anomalous transport [1]. The moderate longitudinal conductivity of $\sigma_{zz}(T = 1.4 \text{ K})$ in the order of 10^5 S cm^{-1} places LuMn_6Sn_6 in the moderate conductivity regime where intrinsic scattering phenomena dominate the AHE. However, the σ_{zy} values increase sharply at low T 's when the field is ramped into the FFM phase, as shown in Fig. 6(b). In fact, Hall conductivity at 1.4 K reaches $11,000 \text{ S cm}^{-1}$, exceeding the intrinsic AHE of e^2/ha by two orders of magnitude. This shows a clear deviation from the conventional scaling relations established for ferromagnets. Such large AHE with electron-scattering origin (extrinsic mechanisms) has been reported in the chiral FM state of MnGe thin films [6]. Equally interesting is the sudden change in the sign of the AHC in the field about $\mu_0 H = 25 \text{ T}$. The field range of these phases are not accessible for neutron diffraction studies. However, by directly comparing the magnetic phase diagram of LuMn_6Sn_6 (Fig. 1) with YMn_6Sn_6 [33, 39], it can be inferred that the magnetic structure at that field magnitude changes from a fan-like (FL) phase to the FFM phase. Our results suggest the need for further theoretical studies on the enhancement of Berry curvature and its relationship to the observed AHE at these field-induced magnetic phases.

3. Topological Hall Effect in phase III (transverse conical spiral, TCS)

We now turn our attention to the magnetic phase III and the possibility of observing the THE in this phase. THE is a hallmark of scalar spin chirality, which is found in skyrmionic lattice such as MnSi [46], Gd_2PdSi_3 [47], and EuAl_4 [52].

By directly comparing the magnetic phase diagrams of LuMn_6Sn_6 and YMn_6Sn_6 [33, 39], and the neutron scattering studies in Ref. [17], it can be concluded that the magnetic structure of this phase is a transverse conical spiral (TCS). Despite the incommensurate noncoplanar spin texture of the TCS phase, THE is not expected due to its zero scalar spin chirality [30, 39]. However, the TCS phase in YMn_6Sn_6 is reported to exhibit a THE [30]. It has been suggested that magnon fluctuations, coupled with the strongly two-dimensional nature of the magnetic exchange, may explain the observed THE in YMn_6Sn_6 [30]. Following this suggestion, we further analyzed the Hall effect data in the TCS phase by parti-

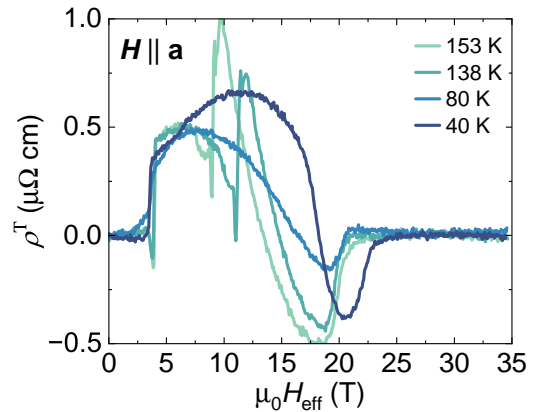


FIG. 7. Extracted topological Hall ρ^T at several constant temperatures within phase III. ρ^T was obtained through the subtraction of anomalous Hall component ρ^A and the ordinary component ρ^O of the Hall resistivity.

tioning it into its major components.

The derived topological contribution to the Hall resistivity in phase III is plotted as a function of effective magnetic field in Fig. 7 (See SM [37] Fig. S6 for detailed calculations). The magnitude of ρ_{zy}^T that we obtained in phase III, after properly accounting for the anisotropy of the longitudinal resistivity, is $0.67 \mu\Omega \text{ cm}$ at 40 K. This is within the reported values of $1 \mu\Omega \text{ cm}$ for YMn_6Sn_6 and ScMn_6Sn_6 [30, 32]. We note that the value of THE would be significantly larger if both longitudinal resistivities were not carefully accounted for in the estimation of the AHE, as we have emphasized in Sec. III C 1. We were unable to clearly separate the contributions of ρ_{zy}^A and ρ_{zy}^T to ρ_{zy} at temperatures below 40 K.

The THE in the Y and Sc compounds is seen at high temperatures, leading to the proposal of a dynamical mechanism as a possible explanation for the appearance of THE in the TCS phase, despite the absence of scalar chirality. In contrast, as shown in Fig. 7, the THE in LuMn_6Sn_6 is observed at a relatively low temperature. In particular, the THE in LuMn_6Sn_6 is exceptionally robust, extending over a 20 T field range. ρ_{zy}^T changes sign in the field ranging around 20 T, before vanishing in the FFM phase. As was pointed out at the end of Sec. III C 2, the magnetic structure at this field range is most likely a FL phase. These peculiar behaviors of THE in LuMn_6Sn_6 suggest the need for further theoretical studies to understand the origin of the emerging THE in the RMn_6Sn_6 family.

IV. CONCLUSION

Our detailed magnetotransport study of the metallic kagome compound LuMn_6Sn_6 reveals a rich magnetic phase diagram driven by competing interactions between multiple magnetic orders under an applied in-plane magnetic field. We identified eight distinct magnetic phases

and uncover an anomalous Hall effect (AHE) in the canted antiferromagnetic (AF1) state, which we attribute to intrinsic contributions. Our analysis also highlights the importance of incorporating anisotropic magnetoresistance in the interpretation of Hall data, and the need for rigorous theoretical frameworks to more accurately interpret the observed Hall responses. Our investigation of the AHE reveals a Hall conductivity of $11,000 \text{ Scm}^{-1}$ at 1.4 K, which exceeds the intrinsic AHE of e^2/ha by two orders of magnitude, despite a moderate longitudinal conductivity σ_{zz} on the order of 10^5 Scm^{-1} . Furthermore, we observe a robust THE in phase III, likely associated with the transverse conical spiral (TCS) magnetic structure. In particular, this THE persists over an exceptionally wide field range of 20 T. Our findings expand the understanding of anomalous transport in antiferromagnetic kagome systems and emphasize the potential of further theoretical studies to fully understand the origin of the AHE and THE in non-collinear antiferromagnetic

compounds.

ACKNOWLEDGMENT

S. M. and D. M. acknowledge the support from the Gordon and Betty Moore Foundation's EPiQS initiative, Grant GBMF9069 and the support from AFOSR MURI Grant No. FA9550-20-1-0322. This publication is funded in part by a QuantEmX grant from ICAM and the Gordon and Betty Moore Foundation through Grant GBMF9616 to Shirin Mozaffari. L. B. is supported by the US Department of Energy (DOE) through the BES program, award DE-SC0002613. The National High Magnetic Field Laboratory is supported by the National Science Foundation through NSF/DMR-1644779 and NSF/DMR-2128556 and the State of Florida.

REFERENCES

-
- [1] N. Nagaosa, J. Sinova, S. Onoda, A. H. MacDonald, and N. P. Ong, Anomalous hall effect, *Reviews of modern physics* **82**, 1539 (2010).
- [2] L. Šmejkal, A. H. MacDonald, J. Sinova, S. Nakatsuji, and T. Jungwirth, Anomalous hall antiferromagnets, *Nature Reviews Materials* **7**, 482 (2022).
- [3] Y. Machida, S. Nakatsuji, S. Onoda, T. Tayama, and T. Sakakibara, Time-reversal symmetry breaking and spontaneous hall effect without magnetic dipole order, *Nature* **463**, 210 (2010).
- [4] S. Nakatsuji, N. Kiyohara, and T. Higo, Large anomalous hall effect in a non-collinear antiferromagnet at room temperature, *Nature* **527**, 212 (2015).
- [5] N. Kiyohara, T. Tomita, and S. Nakatsuji, Giant anomalous hall effect in the chiral antiferromagnet Mn_3Ge , *Physical Review Applied* **5**, 064009 (2016).
- [6] Y. Fujishiro, N. Kanazawa, R. Kurihara, H. Ishizuka, T. Hori, F. S. Yasin, X. Yu, A. Tsukazaki, M. Ichikawa, M. Kawasaki, *et al.*, Giant anomalous hall effect from spin-chirality scattering in a chiral magnet, *Nature communications* **12**, 317 (2021).
- [7] Y. Arai, J. Hayashi, K. Takeda, H. Tou, H. Sugawara, and H. Kotegawa, Intrinsic anomalous hall effect arising from antiferromagnetism as revealed by high-quality nbmnp, *Journal of the Physical Society of Japan* **93**, 063702 (2024).
- [8] H. Kotegawa, H. Tanaka, Y. Takeuchi, H. Tou, H. Sugawara, J. Hayashi, and K. Takeda, Large anomalous hall conductivity derived from an f-electron collinear antiferromagnetic structure, *Physical Review Letters* **133**, 106301 (2024).
- [9] L. Šmejkal, J. Sinova, and T. Jungwirth, Beyond conventional ferromagnetism and antiferromagnetism: A phase with nonrelativistic spin and crystal rotation symmetry, *Physical Review X* **12**, 031042 (2022).
- [10] T. Kida, L. Fenner, A. Dee, I. Terasaki, M. Hagiwara, and A. Wills, The giant anomalous hall effect in the ferromagnet Fe_3Sn_2 -a frustrated kagome metal, *Journal of Physics: Condensed Matter* **23**, 112205 (2011).
- [11] Q. Wang, S. Sun, X. Zhang, F. Pang, and H. Lei, Anomalous hall effect in a ferromagnetic Fe_3Sn_2 single crystal with a geometrically frustrated fe bilayer kagome lattice, *Physical Review B* **94**, 075135 (2016).
- [12] B. P. Belbase, L. Ye, B. Karki, J. I. Facio, J.-S. You, J. G. Checkelsky, J. Van Den Brink, and M. P. Ghimire, Large anomalous hall effect in single crystals of the kagome weyl ferromagnet Fe_3Sn , *Physical Review B* **108**, 075164 (2023).
- [13] M. Ikhlas, T. Tomita, T. Koretsune, M.-T. Suzuki, D. Nishio-Hamane, R. Arita, Y. Otani, and S. Nakatsuji, Large anomalous nernst effect at room temperature in a chiral antiferromagnet, *Nature Physics* **13**, 1085 (2017).
- [14] Y. Zhang, Y. Sun, H. Yang, J. Železný, S. P. Parkin, C. Felser, and B. Yan, Strong anisotropic anomalous hall effect and spin hall effect in the chiral antiferromagnetic compounds mn_3x ($\text{x} = \text{ge, sn, ga, ir, rh, and pt}$), *Physical Review B* **95**, 075128 (2017).
- [15] Q. Wang, Y. Xu, R. Lou, Z. Liu, M. Li, Y. Huang, D. Shen, H. Weng, S. Wang, and H. Lei, Large intrinsic anomalous hall effect in half-metallic ferromagnet $\text{Co}_3\text{Sn}_2\text{S}_2$ with magnetic weyl fermions, *Nature communications* **9**, 1 (2018).
- [16] X. Xu, J.-X. Yin, Z. Qu, and S. Jia, Quantum interactions in topological r166 kagome magnet, *Reports on Progress in Physics* **86**, 114502 (2023).
- [17] S.-H. D. et al., Manuscript in preparation.
- [18] Y. Lee, R. Skomski, X. Wang, P. P. Orth, Y. Ren, B. Kang, A. K. Pathak, A. Kutepov, B. N. Harmon, R. J. McQueeney, I. I. Mazin, and L. Ke, Interplay between magnetism and band topology in the kagome magnets

- $r\text{Mn}_6\text{Sn}_6$, *Phys. Rev. B* **108**, 045132 (2023).
- [19] D. C. Jones, S. Das, H. Bhandari, X. Liu, P. Siegfried, M. P. Ghimire, S. S. Tsirkin, I. Mazin, and N. J. Ghimire, Origin of spin reorientation and intrinsic anomalous hall effect in the kagome ferrimagnet TbMn_6Sn_6 , arXiv preprint arXiv:2203.17246 (2022).
- [20] S. T. Yazdi, N. Tajabor, M. R. Roknabadi, M. Behdani, and F. Pourarian, Magnetoelastic properties of ermn_6sn_6 intermetallic compound, *Journal of magnetism and magnetic materials* **324**, 723 (2012).
- [21] K. Fruhling, A. Streeter, S. Mardanya, X. Wang, P. Baral, O. Zaharko, I. I. Mazin, S. Chowdhury, W. D. Ratcliff, and F. Tafti, Topological hall effect induced by chiral fluctuations in ermn_6sn_6 , *Physical Review Materials* **8**, 094411 (2024).
- [22] T. Asaba, S. M. Thomas, M. Curtis, J. D. Thompson, E. D. Bauer, and F. Ronning, Anomalous hall effect in the kagome ferrimagnet gdmn_6sn_6 , *Physical Review B* **101**, 174415 (2020).
- [23] L. Gao, S. Shen, Q. Wang, W. Shi, Y. Zhao, C. Li, W. Cao, C. Pei, J.-Y. Ge, G. Li, *et al.*, Anomalous hall effect in ferrimagnetic metal RMn_6Sn_6 (R= Tb, Dy, Ho) with clean Mn kagome lattice, *Applied Physics Letters* **119** (2021).
- [24] F. Kabir, R. Filippone, G. Dhakal, Y. Lee, N. Poudel, J. Casey, A. P. Sakhya, S. Regmi, R. Smith, P. Manfrinetti, *et al.*, Unusual magnetic and transport properties in HoMn_6Sn_6 kagome magnet, *Physical Review Materials* **6**, 064404 (2022).
- [25] T. Victa Trevisan and R. McQueeney, High-field magnetic phase diagrams of the $r\text{mn}_6\text{sn}_6$ ($r = \text{gd-tm}$) kagome metals, *Physical Review B* **111**, 054410 (2025).
- [26] G. Venturini, R. Welter, B. Malaman, and E. Ressouche, Magnetic structure of YMn_6Ge_6 and room temperature magnetic structure of LuMn_6Sn_6 obtained from neutron diffraction study, *Journal of alloys and compounds* **200**, 51 (1993).
- [27] G. Venturini, D. Fruchart, and B. Malaman, Incommensurate magnetic structures of RMn_6Sn_6 (R= Sc, Y, Lu) compounds from neutron diffraction study, *Journal of alloys and compounds* **236**, 102 (1996).
- [28] G. Venturini, R. Welter, B. Malaman, and E. Ressouche, Magnetic structure of YMn_6Ge_6 and room temperature magnetic structure of LuMn_6Sn_6 obtained from neutron diffraction study, *Journal of Alloys and Compounds* **200**, 51 (1993).
- [29] A. Matsuo, K. Suga, K. Kindo, L. Zhang, E. Brück, K. Buschow, F. De Boer, C. Lefèvre, and G. Venturini, Study of the mn–mn exchange interactions in single crystals of RMn_6Sn_6 compounds with R= Sc, Y and Lu, *Journal of alloys and compounds* **408**, 110 (2006).
- [30] N. J. Ghimire, R. L. Dally, L. Poudel, D. Jones, D. Michel, N. T. Magar, M. Bleuel, M. A. McGuire, J. Jiang, J. Mitchell, *et al.*, Competing magnetic phases and fluctuation-driven scalar spin chirality in the kagome metal ymn_6sn_6 , *Science Advances* **6**, eabe2680 (2020).
- [31] Q. Wang, K. J. Neubauer, C. Duan, Q. Yin, S. Fujitsu, H. Hosono, F. Ye, R. Zhang, S. Chi, K. Krycka, H. Lei, and P. Dai, Field-induced topological hall effect and double-fan spin structure with a c -axis component in the metallic kagome antiferromagnetic compound Ymn_6sn_6 , *Phys. Rev. B* **103**, 014416 (2021).
- [32] H. Zhang, C. Liu, Y. Zhang, Z. Hou, X. Fu, X. Zhang, X. Gao, and J. Liu, Magnetic field-induced nontrivial spin chirality and large topological Hall effect in kagome magnet ScMn_6Sn_6 , *Applied Physics Letters* **121**, 202401 (2022).
- [33] P. E. Siegfried, H. Bhandari, D. C. Jones, M. P. Ghimire, R. L. Dally, L. Poudel, M. Bleuel, J. W. Lynn, I. I. Mazin, and N. J. Ghimire, Magnetization-driven lifshitz transition and charge-spin coupling in the kagome metal YMn_6Sn_6 , *Communications Physics* **5**, 58 (2022).
- [34] S. Roychowdhury, A. M. Ochs, S. N. Guin, K. Samanta, J. Noky, C. Shekhar, M. G. Vergniory, J. E. Goldberger, and C. Felser, Large room temperature anomalous transverse thermoelectric effect in kagome antiferromagnet YMn_6Sn_6 , *Advanced Materials* **34**, 2201350 (2022).
- [35] R. P. Madhogaria, S. Mozaffari, H. Zhang, W. R. Meier, S.-H. Do, R. Xue, T. Matsuoka, and D. G. Mandrus, Topological nernst and topological thermal hall effect in rare-earth kagome ScMn_6Sn_6 , *Physical Review B* **108**, 125114 (2023).
- [36] Y. Zhu, D. Zhang, G. Zheng, K.-W. Chen, H. Bhandari, K. Jenkins, A. Chan, N. J. Ghimire, and L. Li, Geometrical nernst effect in the kagome magnet $\text{YMn}_6\text{Sn}_4\text{Ge}_2$, *Physical Review B* **110**, 195125 (2024).
- [37] See Supplemental Material at URL will be inserted by publisher for X-ray diffraction analysis, magnetic susceptibility data for the field along the crystalline c -axis, details on building the phase diagram, charge carrier density and mobility, quantum oscillation, and estimation of the topological Hall resistivity. The Supplemental Material also contains Refs. [53–55].
- [38] M. Li, Q. Wang, G. Wang, Z. Yuan, W. Song, R. Lou, Z. Liu, Y. Huang, Z. Liu, H. Lei, Z. Yin, and S. Wang, Dirac cone, flat band and saddle point in kagome magnet ymn_6sn_6 , *Nature Communications* **12**, 3129 (2021).
- [39] R. L. Dally, J. W. Lynn, N. J. Ghimire, D. Michel, P. Siegfried, and I. I. Mazin, Chiral properties of the zero-field spiral state and field-induced magnetic phases of the itinerant kagome metal YMn_6Sn_6 , *Phys. Rev. B* **103**, 094413 (2021).
- [40] H. Zhang, X. Feng, T. Heitmann, A. I. Kolesnikov, M. B. Stone, Y.-M. Lu, and X. Ke, Topological magnon bands in a room-temperature kagome magnet, *Phys. Rev. B* **101**, 100405 (2020).
- [41] E. Rosenfeld and N. Mushnikov, Double-flat-spiral magnetic structures: Theory and application to the RMn_6Sn_6 compounds, *Physica B: Condensed Matter* **403**, 1898 (2008).
- [42] G. Venturini, B. C. El Idrissi, and B. Malaman, Magnetic properties of RMn_6Sn_6 (R= Sc, Y, Gd- Tm, Lu) compounds with HfFe_6Ge_6 type structure, *Journal of magnetism and magnetic materials* **94**, 35 (1991).
- [43] K. Uhlřřová, V. Sechovský, F. de Boer, S. Yoshii, T. Yamamoto, M. Hagiwara, C. Lefèvre, and G. Venturini, Magnetic properties and hall effect of single-crystalline YMn_6Sn_6 , *Journal of Magnetism and Magnetic Materials* **310**, 1747 (2007), proceedings of the 17th International Conference on Magnetism.
- [44] P. K. Das, N. Kumar, R. Kulkarni, S. Dhar, and A. Thamizhavel, Anisotropic magnetic properties and superzone gap formation in cege single crystal, *Journal of Physics: Condensed Matter* **24**, 146003 (2012).
- [45] A. Kitaori, N. Kanazawa, T. Yokouchi, F. Kagawa, N. Nagaosa, and Y. Tokura, Emergent electromagnetic induction beyond room temperature, *Proceedings of the National Academy of Sciences* **118**, e2105422118 (2021).

- [46] A. Neubauer, C. Pfleiderer, B. Binz, A. Rosch, R. Ritz, P. G. Niklowitz, and P. Böni, Topological hall effect in the a phase of mnsi, *Phys. Rev. Lett.* **102**, 186602 (2009).
- [47] T. Kurumaji, T. Nakaajima, M. Hirschberger, A. Kikkawa, Y. Yamasaki, H. Sagayama, H. Nakao, Y. Taguchi, T.-h. Arima, and Y. Tokura, Skyrmion lattice with a giant topological hall effect in a frustrated triangular-lattice magnet, *Science* **365**, 914 (2019).
- [48] T. Kurumaji, S. Fang, L. Ye, S. Kitou, and J. G. Checkelsky, Metamagnetic multiband hall effect in ising anti-ferromagnet erga2, *Proceedings of the National Academy of Sciences* **121**, e2318411121 (2024).
- [49] G. Kimbell, C. Kim, W. Wu, M. Cuoco, and J. W. Robinson, Challenges in identifying chiral spin textures via the topological hall effect, *Communications Materials* **3**, 19 (2022).
- [50] C. Kittel, *Solid state physics*, Vol. 3 (Shell Development Company Emeryville, 1955).
- [51] T. Miyasato, N. Abe, T. Fujii, A. Asamitsu, S. Onoda, Y. Onose, N. Nagaosa, and Y. Tokura, Crossover behavior of the anomalous hall effect and anomalous nernst effect in itinerant ferromagnets, *Physical review letters* **99**, 086602 (2007).
- [52] R. Takagi, N. Matsuyama, V. Ukleev, L. Yu, J. S. White, S. Francoual, J. R. Mardegan, S. Hayami, H. Saito, K. Kaneko, *et al.*, Square and rhombic lattices of magnetic skyrmions in a centrosymmetric binary compound, *Nature communications* **13**, 1472 (2022).
- [53] J. Rodríguez-Carvajal, Recent advances in magnetic structure determination by neutron powder diffraction, *Physica B: Condensed Matter* **192**, 55 (1993).
- [54] D.-X. Chen, E. Pardo, and A. Sanchez, Demagnetizing factors of rectangular prisms and ellipsoids, *IEEE Transactions on Magnetics* **38**, 1742 (2002).
- [55] R. Prozorov and V. G. Kogan, Effective demagnetizing factors of diamagnetic samples of various shapes, *Physical review applied* **10**, 014030 (2018).

Robust Topological Hall in commensurate phase of LuMn_6Sn_6

Shirin Mozaffari,^{1,*} Seung-Hwan Do,¹ Richa Madhogaria,¹ Aikaterini Flessa Savvidou,² Brian Casas,² William R. Meier,¹ Rui Xue,³ Eun Sang Choi,² Luis Balicas,² and David G. Mandrus^{1,3,†}

¹*Department of Materials Sciences and Engineering,
The University of Tennessee, Knoxville, TN 37996, USA*

²*National High Magnetic Field Laboratory, Florida State University, Tallahassee, Florida 32310, USA*

³*Department of Physics and Astronomy, The University of Tennessee, Knoxville, TN 37996, USA*

S1. POWDER X-RAY DIFFRACTION

Powder X-Ray Diffraction measurements were performed on ground crystals in a Panalytical Empyrean diffractometer with $\text{Cu } K_\alpha$ X-ray source. Refinement with FullProf [?], Figs. S1 (a) revealed that LuMn_6Sn_6 has a $P6/mmm$ HfFe_6Ge_6 -type structure.

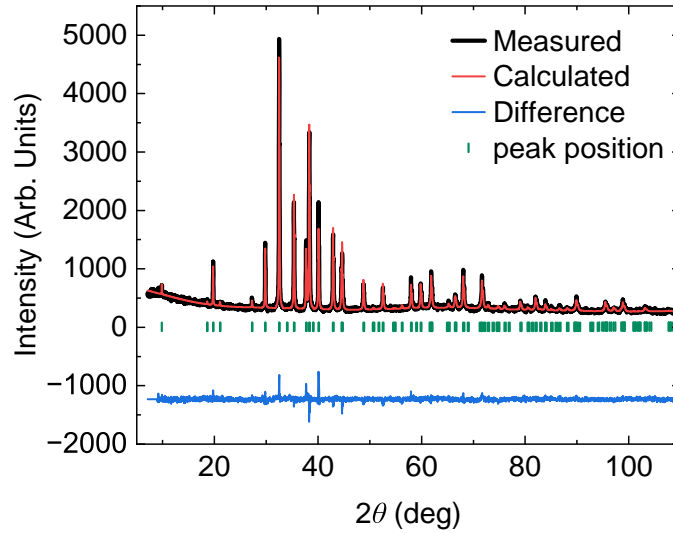


FIG. S1. Powder x-ray diffraction refinement of crushed LuMn_6Sn_6 single crystals using $\text{Cu } K_\alpha$ radiation.

* smozaff1@utk.edu
† dmandrus@utk.edu

S2. MAGNETIC SUSCEPTIBILITY

Magnetic susceptibility (χ) in Fig. S2 reveals two antiferromagnetic phase transitions occurring at $T_{N1} = 394$ K and $T_{N2} = 273$ K. These transition temperatures change by the application of stronger field and are slightly different from those in which the field was applied parallel to the a -axis [Fig 3(a)].

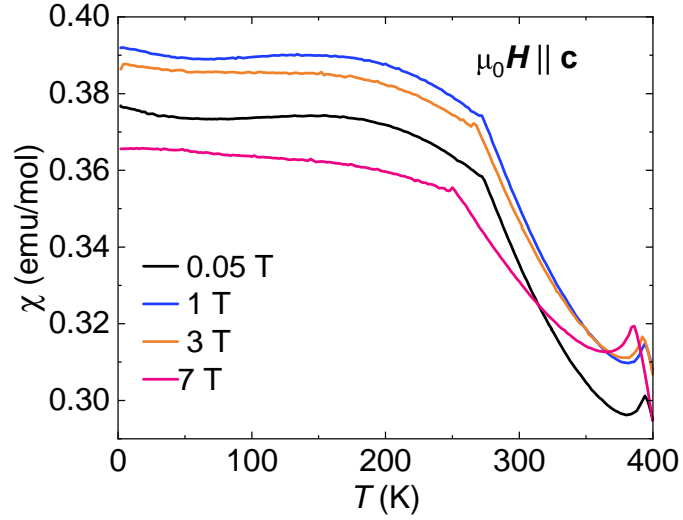


FIG. S2. Temperature dependence of the magnetic susceptibility, for applied field $\mu_0 H$ along the c -axis for LuMn_6Sn_6 , obtained on heating the sample after zero-field-cooling.

S3. TEMPERATURE AND MAGNETIC FIELD PHASE DIAGRAM

The derivative of magnetization and electrical transport data with respect to magnetic field was used to construct the magnetic phase diagram in Fig. 1 in the main text. This is shown for a few representative temperatures in Fig. S3. Similar procedure was performed for the temperature derivative of $M(T)$ curves.

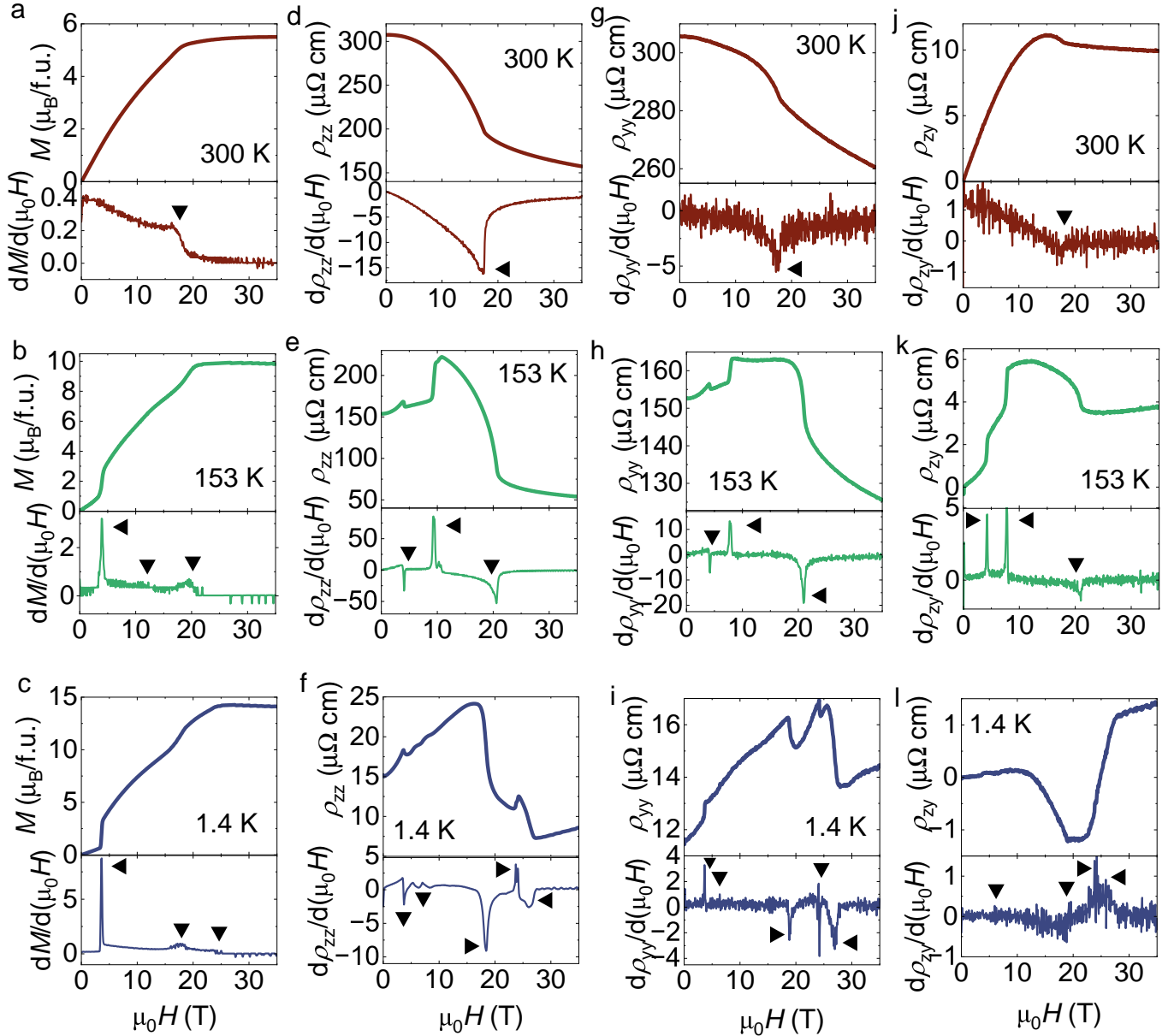


FIG. S3. (a), (b), are (c) Magnetization at 300 K, 153 K, and 1.4 K, respectively, as a function of magnetic field. (d), (e), and (f) are the field dependence of out-of-plane longitudinal resistivity, ρ_{zz} , at 300 K, 153 K, and 1.4 K, respectively. (g), (h), and (i) are the field dependence of in-plane longitudinal resistivity, ρ_{yy} , at 300 K, 153 K, and 1.4 K, respectively. (j), (k), and (l) are the field dependence of Hall effect resistivity, ρ_{zy} , at 300 K, 153 K, and 1.4 K, respectively. The corresponding field derivatives is displayed below each plot. Triangles mark the position of magnetic phase transition on the derivatives curves.

S4. CHARGE CARRIER DENSITIES AND MOBILITIES

A rough estimation for the charge carrier densities n and mobilities μ for holes was performed by fitting low-field Hall resistivity and magnetoresistivity data to the Drude model. The results are shown in Fig. S4. The positive slope of the Hall resistivities data at low fields [Fig. 4(b)] indicates that hole-type carriers dominate the transport. The slope of the Hall resistivity becomes smaller at lower temperatures.

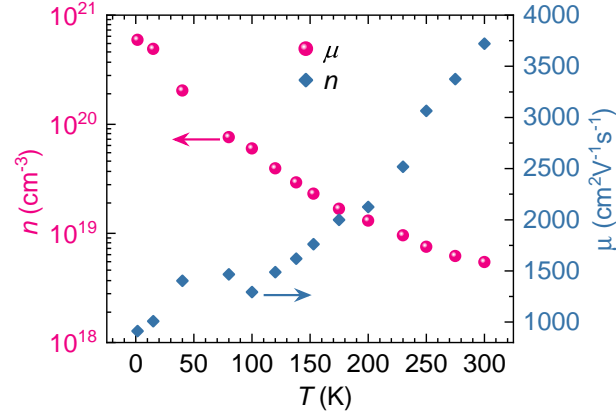


FIG. S4. A rough estimation of the charge carrier densities n and mobilities μ for holes as a function of temperature.

S5. QUANTUM OSCILLATION

LuMn_6Sn_6 showed clear Shubnikov-de Haas (SdH) oscillations 1.4 K. The oscillations are clearer in the FFM phase $\mu_0 H > 27$ T aligned along the a -axis. We analyzed the oscillations by subtracting a smooth polynomial background, and performing a fast Fourier transform (FFT) to get the component frequencies. The peak at 754 T in Fig. S5 corresponds to the extremal cross-sectional areas of the Fermi surface (FS). We used the Onsager relation $F = (\phi_0/2\pi^2)A_k$ to convert the FFT frequencies to reciprocal-space orbit crosssection. $\phi_0 = 2.07 \times 10^{-15} \text{ Tm}^2$ is the flux quantum, and A_k is the cross-sectional area of the FS normal to the applied field. A frequency of 754 T implies a FS pocket that encloses a k -space area (in the bc -plane) of $A_k = 7.2 \text{ nm}^{-2}$. This is 10% of the Brillouin zone of area $4\pi^2/bc = 76.9 \text{ nm}^{-2}$.

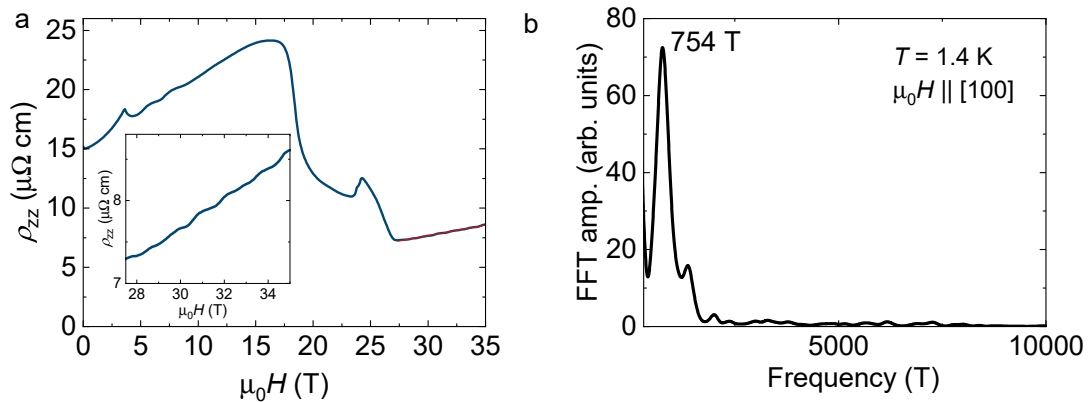


FIG. S5. (a) Magnetic field dependence of longitudinal resistivity at 1.4 K. The red line represents a linear fit in the FFM phase, where the oscillations are more pronounced. The inset provides a zoomed-in view of the high-field range. (b) Fast Fourier transform (FFT) of the oscillatory component of ρ_{zz} .

S6. ESTIMATION OF TOPOLOGICAL HALL RESISTIVITY

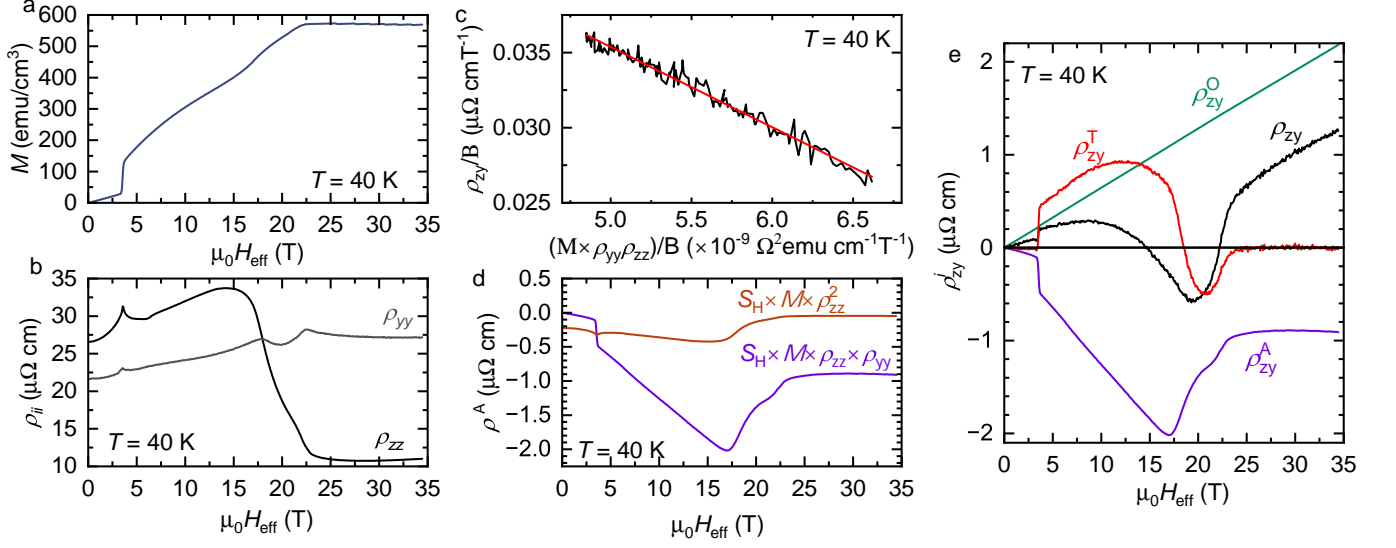


FIG. S6. Estimation of topological Hall resistivity at 40 K for LuMn₆Sn₆. (a) and (b) show the field dependence of magnetization M , in-plane (ρ_{yy}) and out-of-plane (ρ_{zz}) longitudinal resistivity, at $T = 40$ K for $\mathbf{H} \parallel a$. (c) $\frac{\rho_{zy}}{B}$ vs. $\frac{M}{B} \rho_{yy} \rho_{zz}$ curve at the forced ferromagnetic phase $\mu_0 H > 25$ T. Red line is a linear fit to the experimental data. The intercept and slope correspond to R_0 and S_H , respectively. (d) Comparison of the anomalous Hall contribution obtained by $\rho^A = S_H M \rho_{zz}^2$ and $S_H M \rho_{yy} \rho_{zz}$, where the impact of anisotropy is considered. (e) Estimated different components of ρ_{zy} . Curve labeled as ρ_{zy} is the total Hall resistivity measured at 40 K. ρ_{zy}^O and ρ_{zy}^A are the normal Hall resistivity estimated from $R_0 B$, and the anomalous Hall resistivity estimated from $S_H M \rho_{yy} \rho_{zz}$. ρ_{zy}^T is the topological Hall resistivity derived from $\rho_{zy}^T = \rho_{zy} - \rho_{zy}^O - \rho_{zy}^A$.

For a noncoplanar magnetic metal, the empirical relation for the Hall effect resistivity is

$$\rho_{zy} = \rho_{zy}^O + \rho_{zy}^A + \rho_{zy}^T = R_0 B + S_H M \rho_{yy} \rho_{zz} + \rho_{zy}^T \quad (1)$$

The first term is the ordinary Hall effect ($\rho_{zy}^O = R_0 B$) due to the Lorentz force. R_0 is ordinary Hall coefficient and $B = \mu_0(H_{\text{eff}} + M)$ is the induction field. $\mu_0 H_{\text{eff}} = \mu_0(H - N_d M)$ is the effective magnetic field and N_d is the demagnetizing factor of the sample and can be estimated from Ref. [? ?]. ρ^A is the anomalous Hall resistivity, and S_H is a constant. The last term ρ_{zy}^T represents the topological Hall resistivity.

At sufficiently high magnetic fields, in the forced ferromagnetic phase where the system is fully polarized, $\rho_{zy}^T = 0$. R_0 and S_H can be extracted in this regime by dividing both sides of Eq. 1 by B ,

$$\frac{\rho_{zy}}{B} = R_0 + S_H \frac{M}{B} \rho_{yy} \rho_{zz} \quad (2)$$

We plot the relationship between $\frac{\rho_{zy}}{B}$ vs. $\frac{M}{B} \rho_{yy} \rho_{zz}$ for scaling analysis. A representative curve at $T = 40$ K is shown in Fig. S6(c). R_0 and S_H were determined from the intercept and slope of the linear fit, respectively. ρ^T was estimated after the subtraction of ρ_{zy}^O and ρ^A from ρ_{zy} as shown in Fig. S6(e). As pointed out in the main text, the field dependence of the in-plane (ρ_{yy}) and out-of-plane (ρ_{yy}) resistivity are distinct, as shown in Fig. S6(b). Fig. S6(d) further illustrates that if the anisotropy of magnetoresistivity is neglected and $\rho^A = S_H M \rho_{zz}^2$ is assumed, the resulting anomalous Hall effect will be much smaller, leading to an overestimation of the topological Hall effect. Moreover, we observe that employing the empirical relation $\rho^A = S_H M$ results in an even greater overestimation.

REFERENCES